

cambridge.org/mrf

Zhenhua Li

Network and Education Technology Center, Yichun University, Yichun, Jiangxi, 336000, China

## Research Paper

**Cite this article:** Li Z (2023). Modeling and electromagnetic analysis of typical environmental clutter based on SMCG. *International Journal of Microwave and Wireless Technologies* **15**, 322–330. <https://doi.org/10.1017/S1759078722000496>

Received: 31 July 2021  
Revised: 22 March 2022  
Accepted: 29 March 2022  
First published online: 26 April 2022

### Keywords:

Bandwidth; grass surface; long tail; probability density function; scattering

### Author for correspondence:

Zhenhua Li, E-mail: [zhenhuali\\_01@126.com](mailto:zhenhuali_01@126.com)

## Abstract

In the research of the natural ecological environment, environmental scattering is an important research content whose results are widely used. In order to fully study the relevant characteristics of the natural grassland environment, this paper established a grassland broadband clutter model, summarized the dominant and recessive laws of the grassland environment broadband clutter, and provided a new perspective for related environmental monitoring which would be helpful to solve the problem of target detection in complex environments. The main work of this paper is as follows: The dielectric constant model of the grass was established, and the curve of the dielectric constant with frequency was obtained. The Monte Carlo method combined with the Gaussian spectrum function was used to generate a two-dimensional Gaussian surface to simulate the actual grass surface. A broadband clutter model was established, and, considering the calculation efficiency and accuracy, the Sparse Matrix/Canonical Grid (SMCG) was used to calculate the surface scattering coefficient. Then, the environmental clutter amplitude with different radar bandwidth (10, 40, 80 MHz), surface roughness ( $h = 0.1$  m,  $h = 0.2$  m,  $h = 0.4$  m) and grazing angle ( $30^\circ$ ,  $60^\circ$ ) were calculated and the probability density function (PDF) was obtained. The results show that the higher the radar resolution, the larger the incident angle, and the rougher the interface, all of which will cause the tail of the PDF to become longer which will not only reduce the detection probability of the radar, but also the tracking accuracy. The research results can be used for civilian and military field.

## Introduction

Grassland is an important natural resource and ecosystem, dominated by herbs, the material basis for economic development in grassland pastoral areas and the most basic means of production for herders. However, due to the long-term over-cultivation, over-grazing and other reasons, the desertification and degradation of the grasslands have become more serious, which has had a great impact on the civilian and even military aspects.

With the rapid development of modern radar technology [1, 2], the radar's detection range and recognition accuracy have improved significantly, which has dealt a heavy blow to high-speed penetration weapons, making them lose their initial advantages. To this end, almost all countries put more energy into the research of grassland ultra-low-altitude penetration technology [3, 4] and a batch of ultra-low-altitude penetration weapons capable of flying about 100 meters in mountainous areas and 15 meters in plains, such as grasslands, has been developed. When the aircraft performs ultra-low-altitude penetration, the echo received by the radar consists of two parts, one is the scattered echo of the ultra-low-altitude target aircraft, and the other is environmental clutter. The complex echoes make it difficult for radars to process information efficiently. As a result, the detection capability of the radar decreased sharply.

To solve this problem, a comprehensive understanding of environmental clutter is required. Only when subtle differences can be found in the clutter echoes can the radar system [5, 6] be kept in the best condition to capture the enemy's trajectory at any time. At the same time, the study of environmental clutter is also of great significance in remote sensing [7–9]: Environmental echoes contain rich information such as surface temperature, soil moisture, soil dielectric constant, seawater salinity, crop type, crop growth and imaging, etc. Correctly processing environmental echoes and extracting information has great application value in military and civilian fields.

A large number of scholars have done a lot of work on the characteristics of environmental clutter [10]: In order to suppress the sea clutter and ionosphere clutter received in the main lobe direction of the antenna, a main lobe clutter suppression method based on a single notch filter is proposed in reference [11] which made an important contribution to target detection and tracking. In order to effectively extract target information from environmental clutter, reference [12] proposes a method to distinguish the target from the clutter effectively at high frequency, but when the target radial velocity is not zero, the method is no longer effective. In reference [13], the first-order clutter spectrum of High-Frequency Surface Wave Radar

(HFSWR) with the influence of the marine environment is studied. In reference [14], a three-partitioned random multiplicative model is adopted to simulate multifractal sea clutter, and the similar multiplication factor of Ice Multiparameter Imaging X-Band (IPIX) radar sea clutter is adopted to construct the multifractal sequence whose spectrum is calculated by using the Qth-order moment structure partition function (QMSPF). In reference [15], the two-dimensional direct numerical simulation method is used to study the statistical characteristics of sea clutter at 85° incident angle, and the influence of wind speed, radar resolution on it is discussed, but there is no further study on the statistical characteristics of sea clutter at a low incident angle.

However, there is abundant evidence that there is no complete study of the statistical characteristics of grassland environmental clutter. This paper discusses the scattering characteristics of grassland environmental clutter from a new perspective, and studies the effects of different bandwidths and incident angles on grassland environmental clutter. Comprehensively discuss the influence of grassland environmental clutter characteristics on roughness, and solve the problem of radar detection of ultra-low altitude targets. It is found that with the increase of radar resolution, rough surface roughness and incident angle, the smearing phenomenon of clutter amplitude probability density becomes more serious. This is consistent with the research results in [13] and verifies the correctness of the results in this paper.

### Model of effective relative permittivity in grassland

Grassland is the main vegetation in nature, covers a wide area, and has various functions such as regulating climate, maintaining ecological balance, and preventing soil desertification. The grass is a mixture, mainly composed of grass bulk material, free water and bound water and the amount of water in it has a great influence on its dielectric constant which is used to be calculated by Debye-Cole Double-frequency Scattering Model [16]:

$$\epsilon_v = v_r \epsilon_r + v_{bw} \epsilon_{bw} + v_{fw} \epsilon_{fw} \tag{1}$$

In the formula,  $v_r$  represents the percentage of grass bulk materials, and  $v_{bw}$ ,  $v_{fw}$  is the volume ratio of the combined water and the free water.  $\epsilon_r$ ,  $\epsilon_{bw}$ ,  $\epsilon_{fw}$  represents the dielectric constant of the three, respectively.

$$\epsilon_{fw} = 4.9 + \frac{75.0}{1 + jf/18} - j \frac{18\sigma}{f} \tag{2}$$

$$\epsilon_{bw} = 2.9 + \frac{55.0}{1 + (jf/0.18)^{0.5}} \tag{3}$$

Bring (2) (3) into (1):

$$\begin{aligned} \epsilon_v = & v_r \epsilon_r + v_{bw} \left( 2.9 + \frac{55.0}{1 + (jf/0.18)^{0.5}} \right) \\ & + v_{fw} \left( 4.9 + \frac{75.0}{1 + jf/18} - j \frac{18\sigma}{f} \right) \end{aligned} \tag{4}$$

The volume content of plant material in the formula ( $v_r$ ) is generally less than 1.0%, and the other parameters  $\epsilon_r$ ,  $v_{bw}$  and  $v_{fw}$  are mainly related to the mass water content, which can be

expressed as [16]

$$\epsilon_r = 1.7 - 0.74 m_g + 6.16 m_g^2 \tag{5}$$

$$v_{bw} = 4.64 m_g^2 / (1 + 7.36 m_g^2) \tag{6}$$

$$v_{fw} = m_g (0.55 m_g - 0.076) \tag{7}$$

In the formula,  $m_g$  is mass water content whose value range is 0.04–0.68.

In many data tests, it is found that when the model is applied to non-corn leaf vegetation materials, the use of volumetric water content  $m_v$  instead of mass water content  $m_g$  can effectively reduce the error, which can be expressed as  $m_v = m_g \rho / [1 - m_g (1 - \rho)]$ .  $\rho$  is the soil density, and the expression for other values of  $m_v$  is [16]:

$$\epsilon_r = 1.7 - 3.2 m_v + 6.5 m_v^2 \tag{8}$$

$$v_{fw} = m_v (0.82 m_v - 0.166) \tag{9}$$

$$v_{bw} = 31.4 m_v^2 / (1 + 59.5 m_v^2) \tag{10}$$

The variation curve of the effective dielectric constant of straw with frequency is shown in Fig. 1. The percentage of moisture represents the water content of the grass, the abscissa represents the frequency of the incident wave, and the ordinate represents the dielectric constant (real and imaginary parts). Obviously, as the moisture content increases, the effective dielectric constant of the grass increases greatly. Conversely, the dielectric constant decreases as the frequency increases.

### Rough surface modeling and scattering calculation

#### Rough surface modeling

The rough surface height profile function  $f(x, y)$  combined with FFT can be expressed as [17]

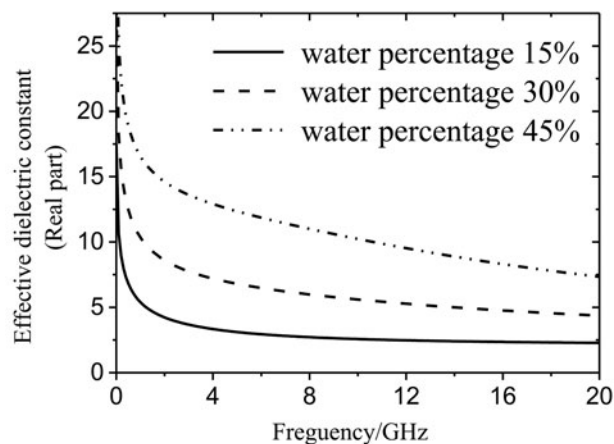
$$f(x, y) = \frac{1}{L_x L_y} \sum_{m=-\infty}^{\infty} \sum_{n=-\infty}^{\infty} b_{mn} \exp\left(\frac{j2\pi mx}{L_x}\right) \exp\left(\frac{j2\pi ny}{L_y}\right) \tag{11}$$

In the formula, the coefficient  $b_{mn}$  can be expressed as

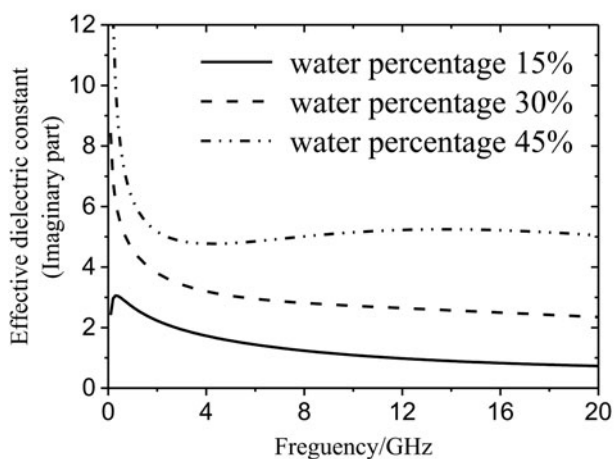
$$\begin{aligned} b_{mn} = & 2\pi \sqrt{L_x L_y} W(k_{xm}, k_{ym}) \cdot \\ & \begin{cases} \frac{N(0, 1) + jN(0, 1)}{\sqrt{2}} & m \neq 0, N_x/2, n \neq 0, N_y/2 \\ N(0, 1) & m = 0, N_x/2 \text{ or } n = 0, N_y/2 \end{cases} \end{aligned} \tag{12}$$

The Gaussian spectral function  $W(k_{xm}, k_{ym})$  is expressed as

$$W(k_{xm}, k_{ym}) = \frac{L_x L_y h^2}{4\pi} \exp\left(-\frac{k_x^2 l_x^2}{4} - \frac{k_y^2 l_y^2}{4}\right) \tag{13}$$



(a)



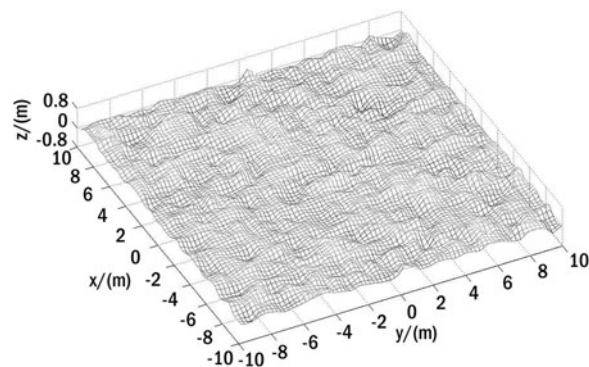
(b)

Fig. 1. Effective dielectric constant of fresh grass. (a) Real part. (b) Imaginary part.

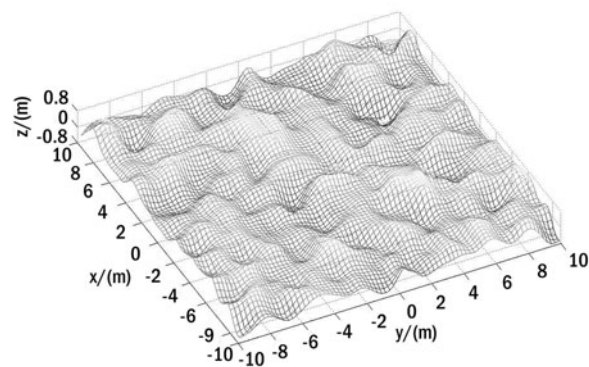
Where  $N(0, 1)$  represents the random sampling point of positive distribution,  $L_x$  and  $L_y$  are the contour length of a rough surface in  $x$  and  $y$  direction. And in formula (13),  $h$  is the root-mean-square height of the Gaussian rough surface,  $l_x$  and  $l_y$  are the correlation length of the rough surface in  $x$  and  $y$  directions.  $N_x$  and  $N_y$  are the number of sampling points of a rough surface in  $x$  and  $y$  directions,  $k_{xm}$  and  $k_{yn}$  are the discrete points of spatial frequency in  $x$  and  $y$  directions which can be expressed as

$$k_{xm} = \frac{2\pi m}{L_x}, \quad k_{yn} = \frac{2\pi n}{L_y} \quad (14)$$

The following two-dimensional Gaussian rough surface is generated by combining the Monte Carlo method and the Gaussian spectrum function. It can be seen that the rough surface becomes rougher as the root-mean-square height of the Gaussian rough surface increases. Different rough surfaces can be generated by assigning different parameter values (Fig. 2).



(a)



(b)

Fig. 2. Rough surface model. (a)  $h = 0.1$  m,  $l_x = l_y = 1.0$  m. (b)  $h = 0.3$  m,  $l_x = l_y = 1.0$  m.

SMCG method based on surface integral equation

The surface integral equation of two-dimensional soil rough surface [18] is

$$n \cdot E_{inc}(r) = \frac{n \cdot E(r)}{2} - n \cdot \left\{ \int_{S_r} j\omega\mu_0 n' \times H(r') g_0(r, r') ds' + P \int_{S_r} [(n' \times E(r')) \times \nabla' g_0(r, r') + \nabla' g_0(r, r') n' \cdot E(r')] ds' \right\} \quad (15)$$

$$n \times H_{inc}(r) = \frac{n \times H(r)}{2} + n \times \left\{ \int_{S_r} j\omega\epsilon_0 n' \times E(r') g_0(r, r') ds' - P \int_{S_r} [\nabla' g_0(r, r') n' \cdot H(r') + (n' \times H(r')) \times \nabla' g_0(r, r')] ds' \right\} \quad (16)$$

$$0 = -\frac{n \times E(r)}{2} - n \times \left\{ \int_{S_r} j\omega\mu_1 n' \times H(r') g_1(r, r') ds' + P \int_{S_r} [(n' \times E(r')) \times \nabla' g_1(r, r') + \nabla' g_1(r, r') \frac{\epsilon_0}{\epsilon_1} n' \cdot E(r')] ds' \right\} \quad (17)$$

$$0 = -\frac{n \cdot H(r)}{2} + n \cdot \left\{ \int_{S_r} j\omega \epsilon_1 n' \times E(r') g_1(r, r') ds' \right. \\ \left. - P \int_{S_r} \left[ \nabla' g_1(r, r') \frac{\mu_0}{\mu_1} n' \cdot H(r') + (n' \times H(r')) \times \nabla' g_1(r, r') \right] ds' \right\} \quad (18)$$

In the formula,  $g_1$  and  $g_0$  represent Green’s function of the two media, soil and air respectively, Other parameters are defined in reference [18] and will not be described here. While the above four-vector integral equations are obtained, they can be further expanded to six scalar integral equations. Combined with the Method of Moment (MOM), The above equations can be transformed into the following equations [19].

$$\sum_{q=1}^6 \sum_{n=1}^N Z_{mn}^{pq} I_n^{(q)} = I_m^{(p)inc} \quad (p = 1, 2 \dots 6) \quad (19)$$

It should be noted that when  $p = 1, 2, 3, I_m^{(p)inc} = 0$ . There will be a lot of unknown parameters in the direct solution process, so an accelerated algorithm is needed to solve the matrix. Therefore, the Sparse Matrix Canonical Grid method (SMCG) [20] united with the Physics-Based Two Grid (PBTG) [21] method was used to solve the problem. The above equation can be written as

$$(Z^{(S)} + Z^{(FS)} + Z^{(w)})x = b \quad (20)$$

In the formula,  $Z^{(w)}$  stand for the far-field weak correlation matrix,  $Z^{(FS)} = Z_0^{(w)}$  is the plane matrix, and  $Z^{(S)}$  represents the near-field strong correlation matrix.

The near and far fields are defined as: when  $\rho_R < r_{db}$  near fields; When  $\rho_R > r_{db}$  far field, where  $\rho_R$  is the distance between two points of the rough surface,  $r_d$  is the distance parameter used to distinguish the far field from the near field.

$$\rho_R = \sqrt{(x - x')^2 + (y - y')^2} \quad (21)$$

Taking  $Z^{(w)}$  to the Taylor series expansion, gets that

$$\epsilon_h^s = \frac{jk_0}{4\pi} \iint \exp(-jk_0\beta') \left\{ [I_x(x', y') \cos\theta_s \cos\phi_s + I_y(x', y') \cos\theta_s \sin\phi_s - I_x(x', y') \frac{\partial f(x', y')}{\partial x'} \right. \\ \left. \sin\theta_s - I_y(x', y') \frac{\partial f(x', y')}{\partial y'} \sin\theta_s \right\} - \eta_0 \{ F_x(x', y') \sin\phi_s - F_y(x', y') \cos\phi_s \} dx' dy' \quad (29)$$

$$\epsilon_v^s = \frac{jk_0}{4\pi} \iint \exp(-jk_0\beta') \left\{ [I_x(x', y') \sin\phi_s - I_y(x', y') \cos\phi_s] + \eta_0 \{ F_x(x', y') \cos\theta_s \cos\phi_s \right. \\ \left. + F_y(x', y') \cos\theta_s \sin\phi_s - F_x(x', y') \frac{\partial f(x', y')}{\partial x'} \sin\theta_s - F_y(x', y') \frac{\partial f(x', y')}{\partial y'} \sin\theta_s \right\} dx' dy' \quad (30)$$

$$Z^{(w)} = \sum_{m=0}^M Z_m^{(w)} \quad (22)$$

Where M is the order. Then the Taylor expansion of the Green function can be expressed as follows

$$G_{0,1}(R) = \frac{(1 - jk_{0,1}R) \exp(jk_{0,1}R)}{4\pi R^3} = \sum_{m=0}^M a_m^{(0,1)}(\rho_R) \left( \frac{z_d^2}{\rho_R^2} \right)^m \quad (23)$$

$$g_{0,1} = \frac{\exp(jk_{0,1}R)}{4\pi R} = \sum_{m=0}^M b_m^{(0,1)}(\rho_R) \left( \frac{z_d^2}{\rho_R^2} \right)^m \quad (24)$$

Where  $g_1$  and  $g_0$  are a Green function of the two media, and  $z_d = f(x, y) - f(x', y')$ .

Using SMCG to solve the matrix equation after the above processing whose process is as follows

$$(Z^{(S)} + Z^{(FS)})x^{(1)} = b \quad (25)$$

$$(Z^{(S)} + Z^{(FS)})x^{(n+1)} = b^{(n+1)} \quad (26)$$

$$b^{(n+1)} = b - Z^{(w)}x^{(n)} \quad (27)$$

In order to obtain the bi-station scattering coefficient of the dielectric rough surface, introduces the two-station scattering coefficient equation [22], whose expression is

$$\sigma_{hv}(\theta_s, \varphi_s) = \frac{|E_h^s|^2}{2\eta P_v^{inc}} \quad (28)$$

Where  $h$  and  $v$  are the polarization mode,  $\theta_s$  is the scattering angle,  $\varphi_s$  is the azimuth angle,  $E_h^s$  is the scattering field, and  $P_v^{inc}$  is the energy of the incident wave.

Substituting the solution of the two-dimensional matrix equation of the dielectric rough surface into equation (28), the bistatic scattering coefficient of the rough surface of the medium can be obtained [22].

### Algorithm validation

In order to verify the correctness of the algorithm in this paper, the Monte Carlo method combined with the Gaussian spectrum function is used to generate Gaussian rough surface during the

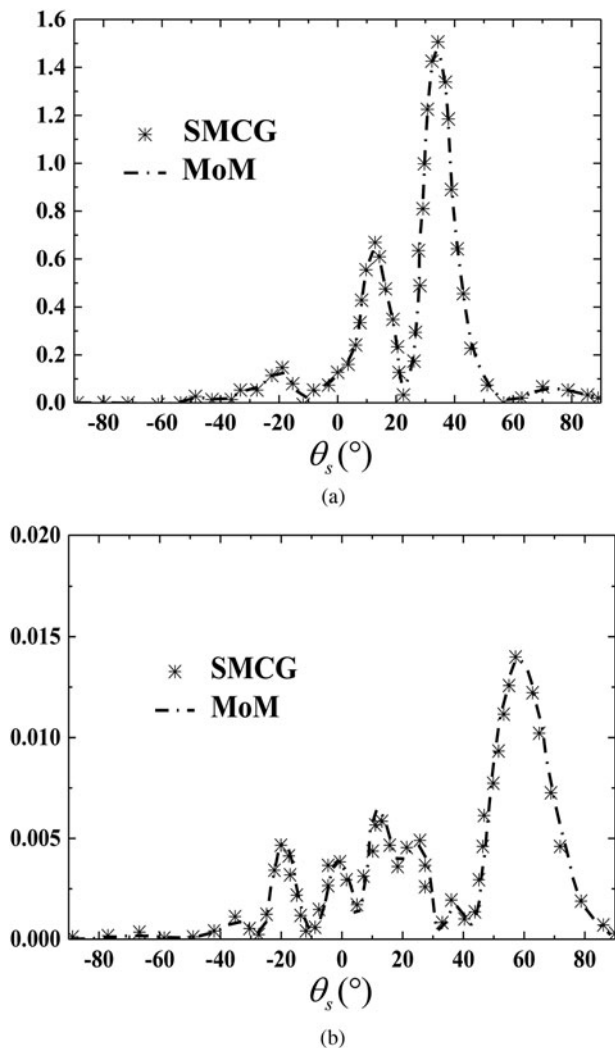


Fig. 3. Validation of algorithm effectiveness. (a) Horizontal polarization. (b) Vertical polarization.

calculation to ensure the consistency of rough surface modeling. Then the SMCG algorithm and the MOM algorithm are used to calculate the scattering coefficient of the rough surface, and the results are plotted in Fig. 3.

Calculation parameters are as follows: root mean square height  $h = 0.2\lambda$ , correlation length  $l_x = l_y = 1.0\lambda$ , effective dielectric constant  $\epsilon = 11.27 + j5.13$ , incidence angle  $\theta_i = 30^\circ$ , the scattering angle varies from  $-90$  to  $90^\circ$ , azimuth angle  $\varphi_i = 0^\circ$ . The projection of the rough surface onto the xoy plane is a square with  $L = 8\lambda$  of each side. Correlation distance  $r_d = 3\lambda$  is used to classify the far field and the near field and the calculation takes the first 6 order of Taylor series expansion.

Figure 3 shows that the results of the algorithm in this paper are basically consistent with those of MOM, indicating the correctness of the algorithm in this paper.

### Simulation and analysis

#### Wideband clutter model

While  $s_t(t)$  and  $s_r(t)$  represent the transmit signal and echo signal of the broadband radar respectively, the echo signal form of the

point target with the broadband condition is as follows [23]:

$$s_r(t) = A \cdot s_t(t - \tau) \tag{31}$$

Where  $A$  and  $\tau$  represent the amplitude factor and transmitting delay respectively. The relative movement between the radar platform and the target will bring a doppler shift  $f_d$  in the echo signal. Considering the Doppler shift, the echo signal  $s_r(t)$  can be expressed as [23]:

$$s_r(t) = A \cdot s_t(t - \tau) \exp(j2\pi f_d(t - \tau)) \tag{32}$$

In this paper, the linear frequency modulation (LFM) signal [24] is taken as an example to study the noise characteristics of wideband radar. The expression of the LFM signal with time width of  $T$  and bandwidth of  $B$  is as follows [25]:

$$s(t) = \text{rect}\left(\frac{t}{T}\right) e^{j2\pi\left(f_0 t + \frac{K}{2}t^2\right)} \tag{33}$$

Where  $\text{rect}(t/T)$  represents the rectangular pulse of time width  $T$ ,  $f_0$  is the radar center frequency, and  $K = B/T$  is the frequency modulation slope.

If the transmitted signal  $s_t(t)$  adopts an LFM signal, equation (33) can be rewritten as

$$s_r(t) = A \cdot \text{rect}\left(\frac{t - \tau}{T}\right) \exp\left[j2\pi\left((f_0 + f_d)(t - \tau) + \frac{K}{2}(t - \tau)^2\right)\right] \tag{34}$$

LFM wideband radar has a relatively high range resolution. When it illuminates the ground and sea environmental background, the environmental background can be divided into many resolution units, and each resolution unit can be regarded as a point target in the processing process [23]. In this way, through vector superposition of the echo signals of all resolution units, the echo signal of the entire ground environment can be obtained. The wideband radar echo signal of a single resolution unit can be expressed as [23]:

$$s_r(t) = A_n \cdot s_t(t - \tau_n) \exp(j2\pi f_d(t - \tau_n)) \tag{35}$$

$A_n$  represents the amplitude factor of the resolution unit [26], which can be obtained according to the radar equation:

$$A_n = \left[ \frac{P_t \lambda^2}{(4\pi)^3 R_n^4 L} \right]^{1/2} \sqrt{\sigma_n^0 S_n} G(\theta) = D \frac{\sqrt{\sigma_n^0 S_n}}{R_n^2} \tag{36}$$

Where  $D$  represents radar parameters, which have nothing to do with the parameters of the resolution unit.  $\lambda$  stands for radar working wavelength,  $P_t$  represents radar transmitting power,  $R_n$  represents the distance between the resolution element and the radar,  $\sigma_n^0$  represents the backscattering coefficient of the resolution element,  $S_n$  represents the area of the resolution element.  $\sigma_n^0 S_n$  is the radar cross section of the resolution element, which can be calculated by the SMCG method in this paper.  $G(\theta)$  represents the direction graph function of the radar antenna, and  $L$  represents the comprehensive loss of the radar system.

When the radar transmit signal  $s_t$  adopts the LFM signal, whose expressions is as in equation (33), the target echo signal

is expressed as

$$s_r(t) = A_n \cdot \text{rect}\left(\frac{t - \tau_n}{T}\right) \exp\left[ (j2\pi(f_0 + f_d)(t - \tau_n) + \frac{K}{2}(t - \tau_n)^2) \right] \quad (37)$$

The above formula is the broadband point target echo model based on the LFM signal.

For broadband radar systems, we can regard the clutter background as a large extended target, and treat each resolution cell as a point target and replace it with a scattering center, so that the background echo signal is the vector of the echo signals of all the scattering centers.

Assuming that there are  $N$  resolution units in total, the broadband background echo signal can be expressed as

$$R_r(t) = \sum_{i=1}^N A_i \cdot s_i(t - \tau_i) \exp(j2\pi f_d(t - \tau_i) + \varphi_i) \quad (38)$$

$A_i$  represents the amplitude factor of the resolution unit, which can be calculated by the formula (36), and  $\varphi_i$  represents the random phase caused by the height fluctuation in the resolution unit. Divide the clutter background into  $M$  equidistant circles ( $M < N$ ) by radial distance at distance resolution intervals, we know that the fixed delays of the echoes of all scattering centers in the equidistant circle are the same, so the broadband background echo signal based on LFM signal is projected on the radial distance, and equation (38) is rewritten as

$$R_r(t) = \sum_{k=1}^N A_k \cdot s_k(t - \tau_k) \exp(j2\pi f_d(t - \tau_k)) \quad (39)$$

Where

$$A_k = \left[ \frac{P_i \lambda^2}{(4\pi)^3 R_k^4 L} \right]^{1/2} \sqrt{\sigma_k^0 S_k G(\theta)} \quad (40)$$

In equations (39) and (40),  $A_k$  represents the amplitude factor after the vector superposition of all the echo signals from the scattering centers in the  $k$ -th distance circle, and  $\tau_k$  represents the transmission and reception delay of the scattering centers in the  $k$ -th equidistant circle.

Based on this, simulation calculation can be carried out to observe the environmental clutter.

### Related parameters of calculation

In the simulation, the size of the ocean rough surface is 500 m × 100 m, which is generated by Gauss spectral function combined with the Monte Carlo method (500 m is the length of the rough surface in the direction of radar wave incidence) (Fig. 4).

According to the broadband clutter model, the environmental clutter echo signal can be calculated. The Fourier transform and pulse compression signal of the environmental clutter time-domain echo signal are further processed, and the clutter spectrum and one-dimensional range image are obtained. The processing method is referred to [26]. It is worth noting that the environmental clutter spectrum simulated in this paper is not the Doppler spectrum of the environment. It is the

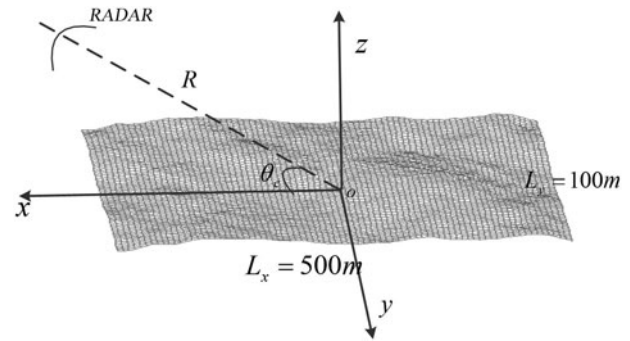


Fig. 4. Schematic diagram of radar wave incidence.  $\theta_c$  represents the grazing Angle,  $R$  is the oblique distance between the center of the environment scene and the radar platform.

environmental clutter spectrum obtained by the Fourier transform processing of the environmental clutter baseband signal in the time domain.

By statistical analysis of the echo signal, the probability density function  $P(r)$  can be obtained, and  $\int_{-\infty}^{+\infty} P(r) dr = 1$ , which can take on in different forms:

In the figure shown above, the higher the value of  $P(r)$ , the higher the probability of  $r$ .

In simulation, the center frequency of the incident wave is 10 GHz, rough surface size is  $l_x \times l_y = 500 \text{ m} \times 100 \text{ m}$ . The grass water content is 45%, and grassland permittivity  $\epsilon = 11.27 + j5.13$ .

### Bandwidth impact

In the process of studying the influence of different bandwidths on clutter characteristics of the grassland environment, the bandwidths are taken as 10, 40 and 80 MHz, respectively, and the grazing angle of incidence is 30°. The results obtained are plotted in four graphs: time-domain sequence curve, spectrum sequence curve, one-dimensional distance graph, and grass clutter probability density graph under different bandwidths, as shown in Fig. 5. Figure 5(a) shows that as the bandwidth increases, the frequency spectrum becomes wider and the echo becomes sharper, but the amplitude does not change much, indicating that the amplitude of the environmental clutter is not limited by the radar bandwidth. The result in Fig. 5(c) shows that the length of the clutter distribution is about 440 m, which is basically the same as the projection length ( $500 \text{ m} \times \cos 30^\circ = 433 \text{ m}$ ) of the environmental scene on the radar line of sight, which verifies the correctness of the simulation results. Figures 5(a) and 5(d) show that there are large fluctuations in the time-domain sequence. For wideband radars with high range resolution, the probability distribution of clutter amplitude presents a long “tail”. This is mainly because, in high-resolution radar, the size of the strong scatterer may be larger than the size of one or more resolution units, resulting in multiple units showing strong scattering characteristics. The appearance of long “tail” will increase the probability of radar false alarm rate, making it difficult for radar to detect, identify and track targets.

### Effect of surface roughness on grass

In order to study the influence of surface roughness on the fluctuation of clutter amplitude, The roughness parameters are set to

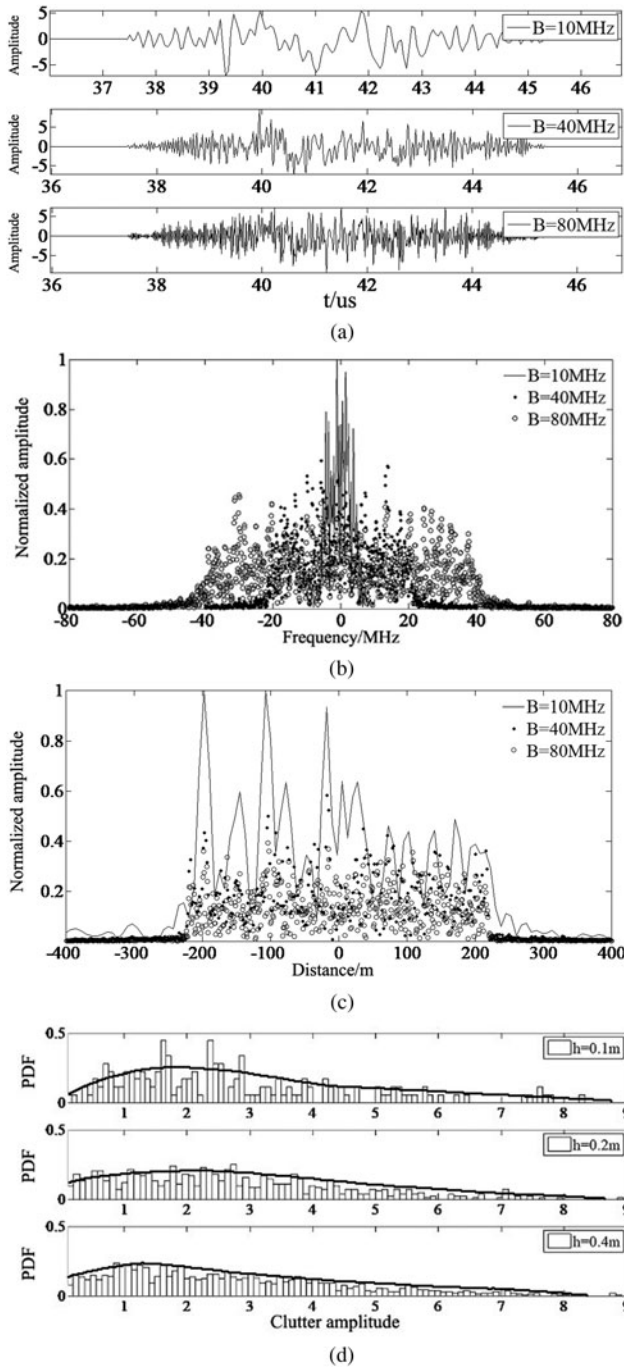


**Fig. 5.** Distribution of grassland clutter in different bandwidths. (a) Time domain sequence. (b) Spectrum characteristics. (c) One-dimensional distance image. (d) Probability density curve.

three values ( $h = 0.1$  m,  $h = 0.2$  m,  $h = 0.2$  m) and discuss the influence of roughness on grass clutter. Other parameters are: bandwidth 50 MHz, glancing angle  $60^\circ$ . In the simulation, the one-dimensional distance image projection interval is about 267 m, which is exactly the same as the projection length of the environment scene ( $500 \text{ m} \times \cos 60^\circ = 250 \text{ m}$ ).

In Figs 6 and 6(a) shows that when the surface roughness of the grass increases, the amplitude of the ground clutter increases. This is because the increase in the roughness of the grass increases the scattering intensity, indicating that the roughness of the

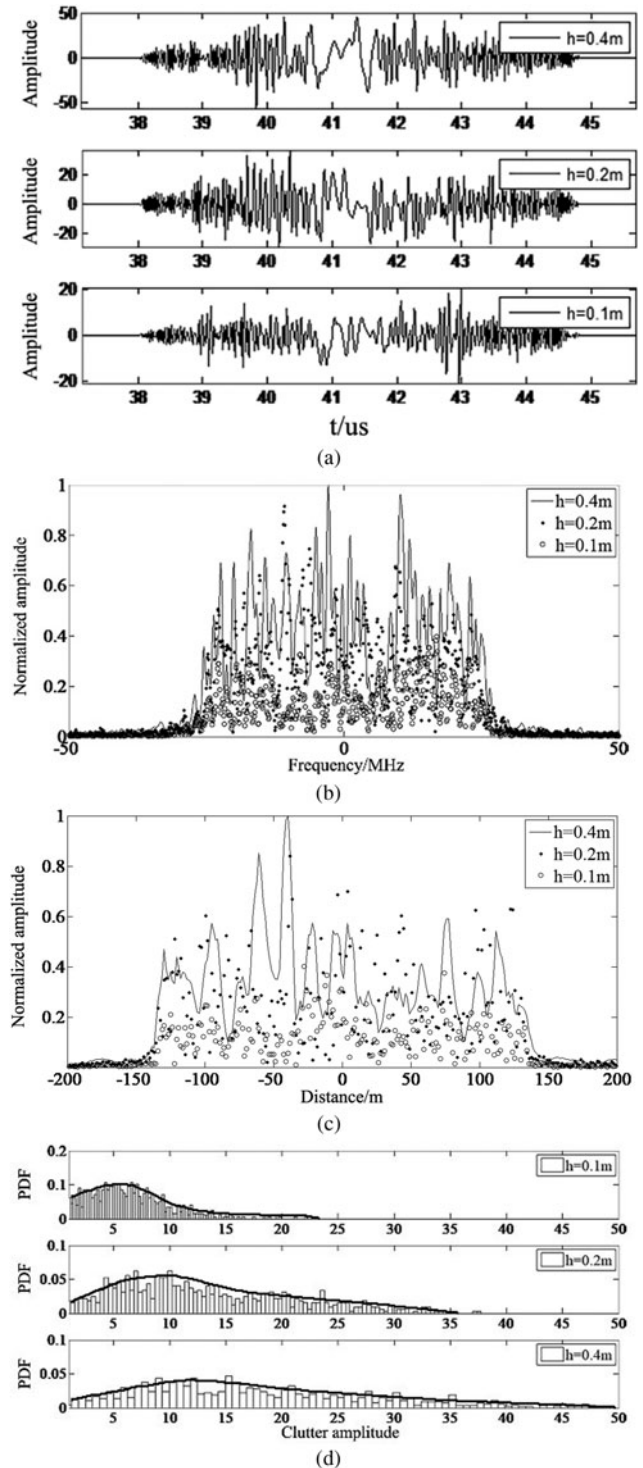


**Fig. 6.** Distribution of grassland clutter in different roughness. (a) Time domain sequences. (b) Spectrum characteristics. (c) One-dimensional distance image. (d) Probability density curve.

environmental surface is one of the important factors affecting clutter. Moreover, in Fig. 6(d), compared with the clutter amplitude distribution of small roughness, the probability density of large roughness is extremely scattered, and there is a very long “tail”, which will lead to the probability of false alarms. The increase makes it more difficult for radar to detect low-altitude penetration aircraft.

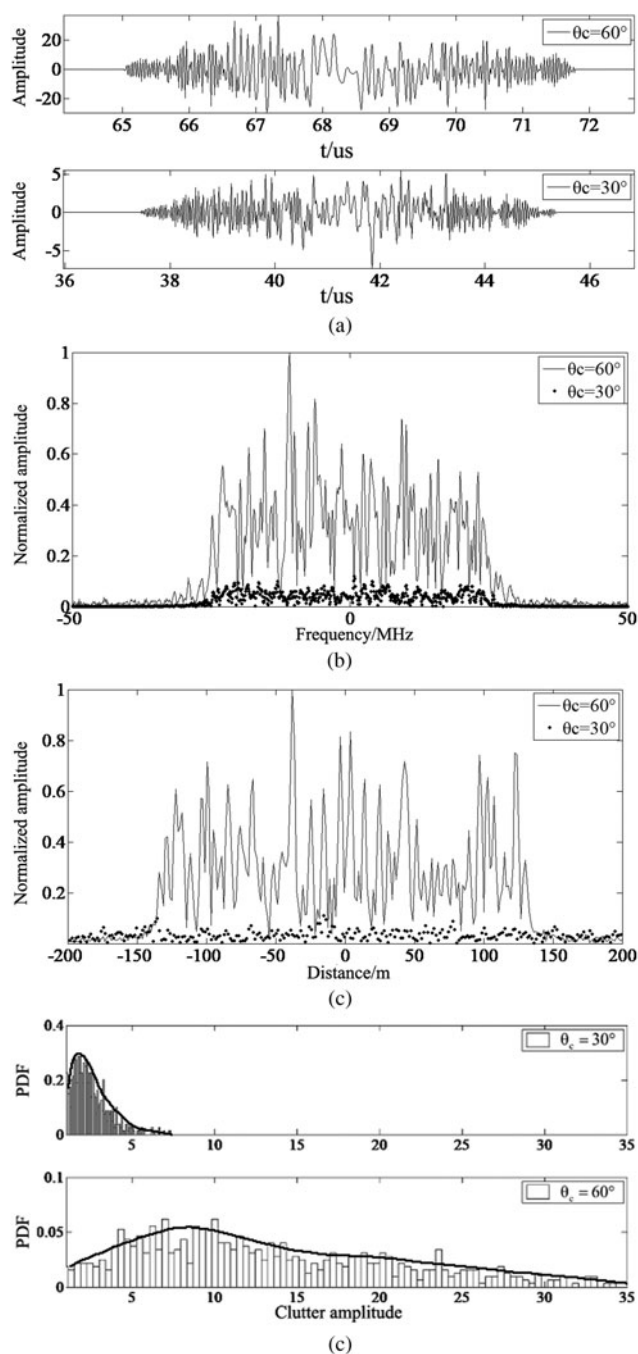


**Fig. 7.** Distribution of grassland clutter in different grazing angles. (a) Time domain sequences. (b) Spectrum characteristics. (c) One-dimensional distance image. (d) Probability density curve.

### Effect of rubbing

When the radar wave is incident at  $30^\circ$  or  $60^\circ$ , the amplitude of the grass clutter is significantly different. It is shown in Fig. 7(a) that as  $\theta_c$  increases, the amplitude of the echo increases, indicating that the grazing angle is an important factor affecting the amplitude of clutter. More importantly, as the grazing angle increases, the “tail” of the clutter probability density becomes longer. At the same time, the amplitude of the clutter increases rapidly, causing the target to be “submerged” in the environmental echo, increasing the probability of false alarms.

However, if the grazing angle of the incident wave is too small, the amplitude of the radar will decrease, causing the echo amplitude to be lower than the radar detection threshold, and the target cannot be found at this time. Therefore, reducing the incident angle of the radar within a certain range can effectively increase the probability of target discovery and improve the accuracy and efficiency of the radar.

### Conclusion

In this paper, a model of grassland effective dielectric constant was established, and the variation curve of grassland effective dielectric constant with frequency was drawn. The two-dimensional rough surface was generated by combining the Monte Carlo method and Gaussian spectrum function, and the SMCG method was used to calculate the scattering coefficient of the rough surface, then the environmental echo was obtained based on the broadband clutter model. The effects of different radar bandwidths, grass roughness and incidence angles on grass clutter were investigated. It is found that with the increase of radar bandwidth, roughness and incident angle, the “tailing” of the probability density of clutter amplitude becomes more serious, resulting in a decrease in radar detection capability. However, further research is needed to determine how to optimize the clutter characteristics and it is necessary to conduct more detailed research. At the same time, this paper does not consider the grassland density, which also has certain limitations. The next step is to build a grassland density model to make theoretical research more practical.

### References

1. Wang DW, Ma XY, Chen AL and Su Y (2010) High-resolution imaging using a wideband MIMO radar system with two distributed arrays. *IEEE Transactions on Image Processing* **19**, 1280–1289.
2. Chen XL, Chen BX, Guan J, Huang Y and He Y (2018) Space-range-Doppler focus-based low-observable moving target detection using frequency diverse array MIMO radar. *IEEE Access* **6**, 43892–43904.
3. De Adana FS, Gonzalez I, Gutierrez O and Catedra MF (2003) Asymptotic method for analysis of RCS of arbitrary targets composed by dielectric and/or magnetic materials. *IEEE Proceedings: Radar, Sonar and Navigation* **150**, 375.
4. Zhou B, Dai HY, Zhang Y and Qiao HD and Xvzhou, Jianguo, China (2018). Validation of Maneuvering Target RCS by Computation based on Feature Selective Validation (FSV). *Presented at 2018 Cross Strait Quad-Regional Radio Science and Wireless Technology Conference (CSQRWC)*. [Online]. Available at <https://ieeexplore.ieee.org/document/8455648>.
5. Wang CY, Su CL, Wu KH and Chu YH (2017) Cross spectral analysis of CODAR-SeaSonde echoes from sea surface and ionosphere at Taiwan. *International Journal of Antennas and Propagation* **2017**, 1–14.
6. Chenguang S, Fei W, Sana S and Jianjiang Z (2018) Low probability of intercept-based radar waveform design for spectral coexistence of distributed multiple-radar and wireless communication systems in clutter. *Entropy: International and Interdisciplinary Journal of Entropy and Information Studies* **20**, 197–201. doi: 10.3390/e20030197.
7. Hu G, Yang Z, Han J, Huang L, Gong J and Xiong N (2018) Aircraft detection in remote sensing images based on saliency and convolution neural network. *EURASIP Journal on Wireless Communications and Networking* **2018**, 1–16.
8. Huang P, Xie SP, Hu K, Huang G and Huang R (2013) Patterns of the seasonal response of tropical rainfall to global warming. *Nature Geoscience* **6**, 357–361.
9. Lin Z (2003) *Simulations of Emissivity in Passive Microwave Remote Sensing with 3-Dimensional Numerical Solutions of Maxwell Equations*



- and *Fast Algorithm* (PhD dissertation). Dept. Elect. Eng., Washington Univ., Washington, USA.
10. **Walsh J, Zhang J and Gill E** (2011) High-frequency radar cross section of the ocean surface for an FMCW waveform. *IEEE Journal of Oceanic Engineering* **36**, 615–626.
  11. **Zhang X, Yang Q, Yao D and Deng W** (2015) Main-lobe cancellation of the space spread clutter for target detection in HFSWR. *IEEE Journal of Selected Topics in Signal Processing* **9**, 1632–1638.
  12. **Zhan J, Ji Y, Chu X, Wang Y and Li M** (2016) Vessel target detection using zero-Doppler spectra of radar echo for high-frequency surface wave radar. *IET Radar Sonar and Navigation* **10**, 1243–1248.
  13. **Cai WH, Xie JH and Sun ML and Qinghuangdao, Hebei, China** (2016) Space-time distribution of the first-order sea clutter in high frequency surface wave radar on a moving shipborne platform. *Presented at 2015 Fifth International Conference on Instrumentation and Measurement, Computer, Communication and Control (IMCCC)*, [Online]. Available at <https://ieeexplore.ieee.org/document/7406080>.
  14. **Xi CP, Xiong G, Yang YH and Chen S** (2019) Simulating multi-fractal sea clutter and surface based on the random multiplicative model. *The Journal of Engineering* **2019**, 7087–7091.
  15. **Toporkov JV and Sletten SMA** (2007) Statistical properties of low-grazing range-resolved sea surface backscatter generated through two-dimensional direct numerical simulations. *IEEE Transactions on Geoscience and Remote Sensing* **45**, 1181–1197.
  16. **Tsang L, Kong LA and Shin RT** (1985) *Theory of Microwave Remote Sensing*. New York: John Wiley&Son.
  17. **Pan G** (2000) *Wavelets in Electromagnetics and Device Modeling*. Wiley-Interscience, 2003.
  18. **Morita N, Kumagi N and Mautz J** (1990) *Integral Equation Methods for Electromagnetics*. Boston: Artech House.
  19. **Peng P, Tong CM, Bao JS, Sun JJ and Li D** (2013) Study on the EM scattering from the earth surface based on the 2D rough surface model. *Journal of Microwaves* **29**, 38–42.
  20. **Li SQ, Chan CH, Xia MY and Tsang L** (2001) Multilevel expansion of the sparse-matrix canonical grid method for tow-dimensional random rough surfaces. *IEEE Trans Antennas Propagation* **49**, 1579–1589.
  21. **Su X, Wu ZS, Wang XB and Dai F** (2016) Backscatter analysis of lossy dielectric sea surface using SMCG-PBTG method-comparison with experimental data. *Journal of Electronics & Information Technology* **38**, 486–494.
  22. **Wang YH, Zhang YM and Guo LX** (2008) Investigation of the scattered field from a two-dimensional dielectric target above the planar surface with a Gaussian beam incidence. *Acta Physica Sinica* **57**, 5529–5535.
  23. **Li ZY** (2013) *The Hardware-in-the-Loop Simulation for Wideband Radar Clutter* (PhD dissertation). Dept. College of Electronic and Information Eng., Nanjing University of Aeronautics and Astronautics, Nanjing, China.
  24. **Meng Z, He HM and Dong L** (2009) Characteristic analysis and simulation of LFM signal. *Ship Electronic Engineering*. **29**, 114–117.
  25. **Whoan SK** (2015) A study on multi-site radar operations based on LFM signal. *The Journal of the Institute of Internet, Broadcasting and Communication* **15**, 113–118.
  26. **Yuan F** (2012) *Modeling and Simulating of Linear Frequency Coded Radar Echoes* (PhD dissertation). Dept. School of Information and Communication Eng., University of Electronic Science and Technology of China, Chengdu, China.



**Zhenhua Li**, graduated from Yichun University in 2005 with a bachelor's degree in engineering, and graduated from Jiangxi Normal University with a master's degree in engineering in 2011. Now he is working in the Network and Education Technology Center of Yichun University with the title of lecturer. His main research directions are electromagnetic compatibility, smart antennas, computational electromagnetics, and computer network security.